Article

Structure

Insight into the Assembly of Viruses with Vertical Single β-barrel Major Capsid Proteins

Graphical Abstract

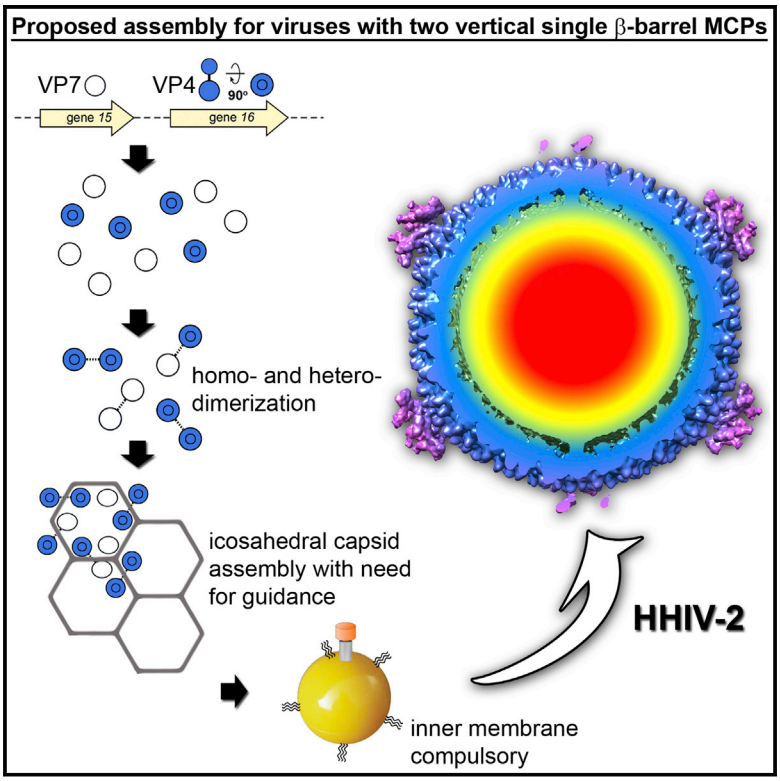

Highlights

- The two capsid proteins of HHIV-2 virus recapitulate vertical single β-barrels
- Disulfide bonds stabilize the virus structure
- Ordered density is visible below the capsid
- Membrane-protein contacts could serve as protein-railings for guiding assembly

Authors

David Gil-Carton, Salla T. Jaakkola, Diego Charro, ..., Hanna M. Oksanen, Dennis H. Bamford, Nicola G.A. Abrescia

Correspondence

nabrescia@cicbiogune.es

In Brief

Gil-Carton et al. present biochemical and structural studies of archaeal, halophilic HHIV-2 virus. The cryo-electron microscopy-based structure shows how membrane-protein interactions below the capsid could serve as protein-railings for guiding the assembly of the two vertical single β-barrel major capsid proteins. Disulfide bonds cement the virus structure.

Gil-Carton et al., 2015, Structure *23*, 1866–1877
October 6, 2015
http://dx.doi.org/10.1016/j.str.2015.07.015

CellPress

Structure
Article

Insight into the Assembly of Viruses with Vertical Single β-barrel Major Capsid Proteins

David Gil-Carton,[1,5] Salla T. Jaakkola,[2,5] Diego Charro,[1] Bibiana Peralta,[1] Daniel Castaño-Díez,[3] Hanna M. Oksanen,[2] Dennis H. Bamford,[2] and Nicola G.A. Abrescia[1,4,*]

[1]Structural Biology Unit, CIC bioGUNE, CIBERehd, Bizkaia Technology Park, 48160 Derio, Spain
[2]Department of Biosciences and Institute of Biotechnology, Viikki Biocenter, University of Helsinki, P.O. Box 56, Viikinkaari 9, 00014 Helsinki, Finland
[3]Scientific Computing Unit, Max-Planck Institute for Brain Research, 60438 Frankfurt, Germany
[4]IKERBASQUE, Basque Foundation for Science, 48013 Bilbao, Spain
[5]Co-first author
*Correspondence: nabrescia@cicbiogune.es
http://dx.doi.org/10.1016/j.str.2015.07.015

SUMMARY

Archaeal viruses constitute the least explored niche within the virosphere. Structure-based approaches have revealed close relationships between viruses infecting organisms from different domains of life. Here, using biochemical and cryo-electron microscopy techniques, we solved the structure of euryarchaeal, halophilic, internal membrane-containing *Haloarcula hispanica* icosahedral virus 2 (HHIV-2). We show that the density of the two major capsid proteins (MCPs) recapitulates vertical single β-barrel proteins and that disulfide bridges stabilize the capsid. Below, ordered density is visible close to the membrane and at the five-fold vertices underneath the host-interacting vertex complex underpinning membrane-protein interactions. The HHIV-2 structure exemplifies the division of conserved architectural elements of a virion, such as the capsid, from those that evolve rapidly due to selective environmental pressure such as host-recognizing structures. We propose that in viruses with two vertical single β-barrel MCPs the vesicle is indispensable, and membrane-protein interactions serve as protein-railings for guiding the assembly.

INTRODUCTION

Structural studies have revealed unexpected evolutionary relationships between bacterial, archaeal, and eukaryotic viruses (Abrescia et al., 2012; Bamford et al., 2005a; Benson et al., 1999). Archaeal viruses occupy unexplored ecological niches, and their three-dimensional (3D) visualizations are few in number. High-resolution structural information (3.9 Å resolution) is currently available for crenarchaeal *Sulfolobus* turreted icosahedral virus (STIV) only (Veesler et al., 2013), whereas another two icosahedral membrane-containing archaeal viruses, STIV2 and SH1, have been characterized at medium resolution (Happonen et al., 2010; Jäälinoja et al., 2008).

Four different structure-based viral lineages have been outlined for viruses displaying icosahedral capsid symmetry (Abrescia et al., 2012; Bamford et al., 2005a). Each of these lineages is characterized by a distinct major capsid protein (MCP) fold and the way it is used to build the virion. MCPs with single horizontal β-barrels are exemplified by rhinovirus and poliovirus where the long axis of the β-barrel is tangential to the virus surface (Hogle et al., 1985; Rossmann et al., 1985). Bluetongue virus type MCPs, with mostly α-helical fold, form a capsid core of 60 homodimers common among double-stranded (ds) RNA viruses (Grimes et al., 1998; Reinisch et al., 2000), whereas the unique HK97 virus MCP fold is seen in herpesviruses, icosahedral tailed phages, and archaeal viruses (Pietilä et al., 2013; Veesler and Cambillau, 2011).

This work focuses on the fourth lineage: the PRD1-adenovirus type viruses. This lineage spans across all three domains of cellular life. Members belonging to this lineage have a capsid lattice made of vertical double β-barrels that trimerize to form pseudo-hexameric capsomers (Abrescia et al., 2012). These viruses are icosahedral and tailless (although PRD1 develops a proteo-lipidic tube for DNA translocation [Peralta et al., 2013]), have dsDNA genomes, and, with the exception of adenovirus, contain an inner membrane. We define these viruses henceforth as "vertical double β-barrel viruses," since there is a single gene encoding an MCP with two contiguous β-barrel domains forming the capsid lattice (Figure 1A).

Recent findings have revealed viruses displaying PRD1-adenovirus type architecture, but with two genes encoding two MCPs, each with a single β-barrel and both composing the lattice (Aalto et al., 2012; Jaakkola et al., 2012; Jäälinoja et al., 2008; Jaatinen et al., 2008; Porter et al., 2013; Zhang et al., 2012) (Figure 1B). We call them hereafter "vertical single β-barrel viruses." To date, all known single β-barrel viruses are prokaryotic and extremophilic. *Thermus* phage P23-77 provides the first example of assembly of an icosahedral capsid lattice made of two MCPs (VP16 and VP17), both possessing a vertical single β-barrel fold (Rissanen et al., 2013). In the P23-77 capsid, VP16 homodimers and VP17 monomers are arranged in pseudo-hexameric capsomers with two-turret morphology (Jaatinen et al., 2008; Rissanen et al., 2013). Both single and double β-barrel viruses encode for a packaging ATPase with a "PRD1 P9-type motif" (Strömsten et al., 2005). In PRD1, this ATPase

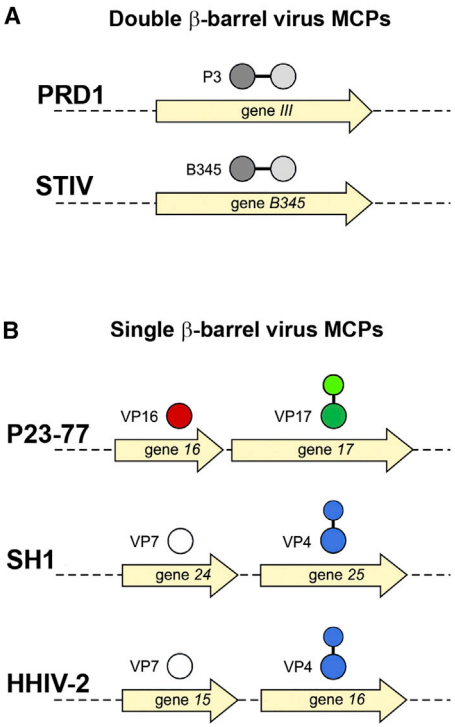

Figure 1. Genetic Context of the Viral Vertical β-Barrel Major Capsid Proteins

(A) One gene (light-yellow arrow) codes for a double β-barrel major capsid protein (MCP) (dark-gray and gray linked circles).

(B) Two adjacent genes code for two different single β-barrel MCPs (individual circles). The genes are drawn to scale. P23-77 MCPs VP16 and VP17 are in red and green, respectively. VP17 is depicted with an additional smaller circle to describe the turret-bearing subunit as shown by the crystal structure (Rissanen et al., 2013). SH1 and HHIV-2 MCPs VP7 and VP4 are in white and slate-blue, respectively.

is shown to power the genome translocation through a unique vertex (Hong et al., 2014; Strömsten et al., 2005).

SH1 was the first isolated icosahedral tailless internal membrane-containing virus of haloarchaea (Euryarchaea) (Porter et al., 2005). Its capsid composed of two MCPs has the same triangulation (*T*) number as P23-77, pseudo $T = 28$, which is unique to these viruses (Jäälinoja et al., 2008; Jaatinen et al., 2008). Unlike in P23-77, SH1 pseudo-hexameric capsomers display two- and three-turret morphologies. Haloarchaeal virus HHIV-2 shares ~59% nucleotide identity with SH1, but has different proteins for interacting with the host cell (Jaakkola et al., 2012).

Here, we combine biochemical and biophysical data with electron microscopy (EM)-based image reconstruction techniques to unravel the structure and assembly of the HHIV-2 virion. The capsid is composed of pseudo-hexameric capsomers with two or three turrets. The capsomers are formed of MCPs VP4 and VP7 that adopt a vertical single β-barrel topology. We also show that disulfide bridges confer HHIV-2 capsid stability. We propose a general principle for the assembly of icosahedral membrane-containing viruses with two single vertical β-barrel MCPs, where the registering of single β-barrels into pseudo-hexameric capsomers onto the membrane vesicle is aided by membrane-protein interactions. Finally, the comparison of HHIV-2 with other viruses shows that the pseudo-hexameric footprint of the capsomers is a unifying feature of the viruses in the PRD1-adenovirus lineage and is not dependent on genome type, capsid assembly mechanism, the number of MCPs, or host-recognizing components.

RESULTS

Quantitative Dissociation of HHIV-2 Capsid- and Membrane-Associated Proteins

Different biochemical conditions were applied to dissociate HHIV-2 particles (see Experimental Procedures and Table S1). Use of urea or guanidine hydrochloride produced quantitative dissociation of the virion with similar results. Three-molar urea, chosen for further experiments, released soluble capsid-associated proteins exposing an inner particle, the lipid core (LC), consisting of the membrane and its associated proteins (see below), but no DNA (Figures 2A and 2B). After the urea treatment, the majority of the HHIV-2 MCPs VP4 and VP7, and the vertex-associating proteins VP2, VP16, and VP17 (half of VP17) were separated from the LC (Figures 2A and 2B). About half of the vertex-associated VP1 was also released (Figures 2A and 2B). Incubation of HHIV-2 in modified SH1 buffer without chloride ions did not result in the release of the vertex complex in HHIV-2 as in the case of SH1 (Jäälinoja et al., 2008). Urea-released proteins were subjected to size-exclusion chromatography (SEC) and rate zonal centrifugation (Figure 2A, lane R) and their masses estimated (Figure S1). SEC suggested the presence of protein complexes, as both MCPs VP4 and VP7 had an apparent mass larger than that of their monomer, although the presence of VP4-VP7 heteromultimers could not be verified. Furthermore, VP7 eluted as two different peaks corresponding to nominal masses of ~70 and 300 kDa (Figure S1). Addition of urea to the SEC analysis did not change the elution profile. HHIV-2 VP2, homologous to SH1 vertex-associated protein VP2 (Jaakkola et al., 2012), migrated slowly, as expected of an elongated protein. VP10 and VP16 had larger apparent masses than expected and eluted in the same fraction, inferring a possible interaction. VP12 was distributed across several fractions possibly as a consequence of attached lipids, which could affect its migration through the column. Analyzed by rate zonal centrifugation assay and SEC, VP16 apparent mass was significantly larger than expected, suggesting multimer formation (Figure S1).

HHIV-2 Capsid Envelopes a Proteo-Lipidic Vesicle

The HHIV-2 LC density was 1.16 g/ml in CsCl. Most abundant LC-associated proteins were VP10 and VP12 (Figure 2A). Proteins VP1, VP5, VP16, VP17, and VP18 were partially LC-associated, with half of them released as soluble by urea (Figures 2A and 2B). HHIV-2 lipid composition differed from that of the host, indicating selective lipid incorporation into the virion during particle assembly, as previously described in other viruses with an inner membrane (Bamford et al., 2005b; Laurinavicius et al., 2004) (Figure S2). None of the HHIV-2 structural proteins contained attached lipids or were glycosylated. The biochemical quantitative dissociation, protein, lipid, and sequence data of HHIV-2, and the available information on SH1 (Jaakkola et al.,

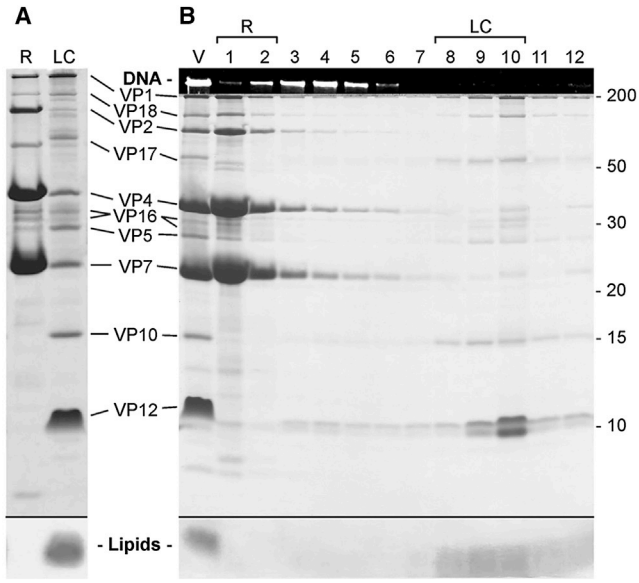

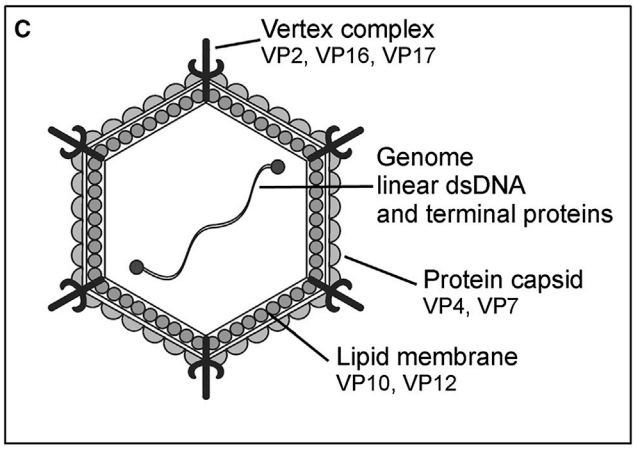

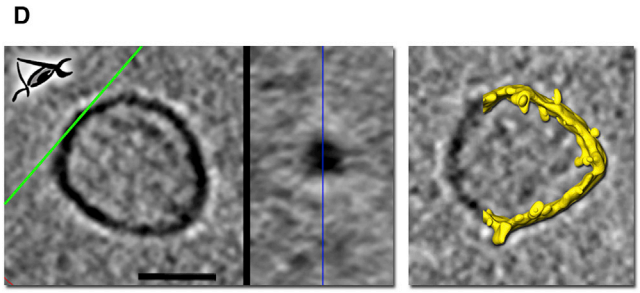

Figure 2. HHIV-2 Dissociation Analysis

(A) HHIV-2 treated with 3 M urea and analyzed by differential centrifugation.

(B) As (A), but analyzed by rate zonal centrifugation. Released proteins (R; the supernatant) are separated from the lipid core (LC; the pellet fraction). Virion proteins (VPs) and lipids analyzed by Coomassie (for proteins) or Sudan Black B (for lipids) stained SDS-PAGE gel (in A and B), and EtBr-stained DNA in the stacking gel of the SDS-PAGE gel (in B). In (B), intact virus (V) is on the left, and evenly fractionated gradient from top to bottom is shown on lanes 1–12 (1/5 of the sample used on lane 1). Standard protein masses (kDa) for (B) are shown on the right, and HHIV-2 proteins for (A) and (B) between the gels.

(C) Schematic representation of the HHIV-2 virion displaying the locations of the major structural proteins.

(D) LCs visualized by cryo-ET. Left: Central section with green line as cutting plane through the cusp formed by the LC surface. Center: Cusp view of the LC from the top at the green cutting plane (eye symbol); blue line bisects the cusp. Right: Segmentation of another LC (yellow) highlights the presence of protuberances emerging from the LC surface.

Scale bar, 15 nm. See also Figures S1 and S2, and Table S1.

2012; Jäälinoja et al., 2008; Kivelä et al., 2006) were used to outline the organization of the HHIV-2 virion prior to its structural analysis by cryo-EM (Figure 2C).

Some of the isolated LCs reconstructed by single-particle cryo-electron tomography (cryo-ET) showed polygonal features with facets that were almost planar (220 Å in length) and formed angles between them (120°–130°) (Figure 2D, left and center). A clear density protruding ~25 Å from the membrane surface likely corresponds to membrane-bound proteins (Figure 2D, right).

HHIV-2 Major Capsid Protein VP7 Monomer-Dimer Switching

HHIV-2 MCPs VP4 (25.9 kDa) and VP7 (19.8 kDa) share greater than 70% sequence identity with the corresponding SH1 VP4 (25.7 kDa) and VP7 (20.0 kDa), but less than 20% with VP17 (31.8 kDa) and VP16 (19.1 kDa) of bacteriophage P23-77. Since SH1 VP4 and VP7 have been proposed to fulfill roles equivalent to those of P23-77 VP17 and VP16 (Rissanen et al., 2013), we analyzed whether structural properties important for assembly, such as order-disorder propensity, would be conserved between HHIV-2 and P23-77 MCPs. Disorder prediction of HHIV-2 VP4 and VP7 depict proteins with higher probability of disorder than the P23-77 VP17 (28% versus 21%) and VP16 (34% versus 19%) (Figure 3A). The VP4 residues from 20 to 43 were predicted to be disordered, which is also true for P23-77 VP17 (Figure 3A). In HHIV-2 VP7, the longest ordered stretch is found in the central part of the sequence, and comprises only ~63 out of 185 residues (Figure 3A). We focused on VP7 because its counterpart P23-77 VP16 has a pivotal role in capsid assembly (Rissanen et al., 2013).

Analysis of recombinant soluble VP7 by SEC coupled to multi-angle light scattering (MALS) in a buffer containing 0.5 M NaCl (buffer A) resulted in two peaks in the elution profile that corresponded to a dimer and a monomer of VP7 (Figure 3B). We also tested the multimericity of VP7 in a high-salt buffer with 1 M NaCl (buffer B), and in buffer A supplemented with a disulfide bond-reducing agent (2 mM Tris-HCl(2-carboxyethyl)phosphine [TCEP]) (buffer C). The elution profile in buffer B replicates that in buffer A (Figure 3B, red and green curves). With TCEP, only the peak corresponding to the monomer remained (Figure 3B, blue curve).

Circular dichroism (CD) spectroscopy of VP7 indicates a protein with ~28% and ~24% of β-sheet and turns, respectively, ~11% of α-helix, and ~36% of residues not assigned to any of the previous structural classes (Figures 3C and S3).

Overall Architecture of HHIV-2 Virion

Cryo-EM reconstruction of HHIV-2 virion at 13 Å resolution as judged by the Fourier shell correlation (FSC) at 0.5 criteria (11 Å at FSC = 0.143; Figure S4) showed an icosahedral internal membrane-containing virus with diameters of ~740 Å (facet to facet), ~775 Å (vertex to vertex), and ~800 Å (edge to edge) (Figures 4A and 4B). The protein capsid and the membrane were ~40

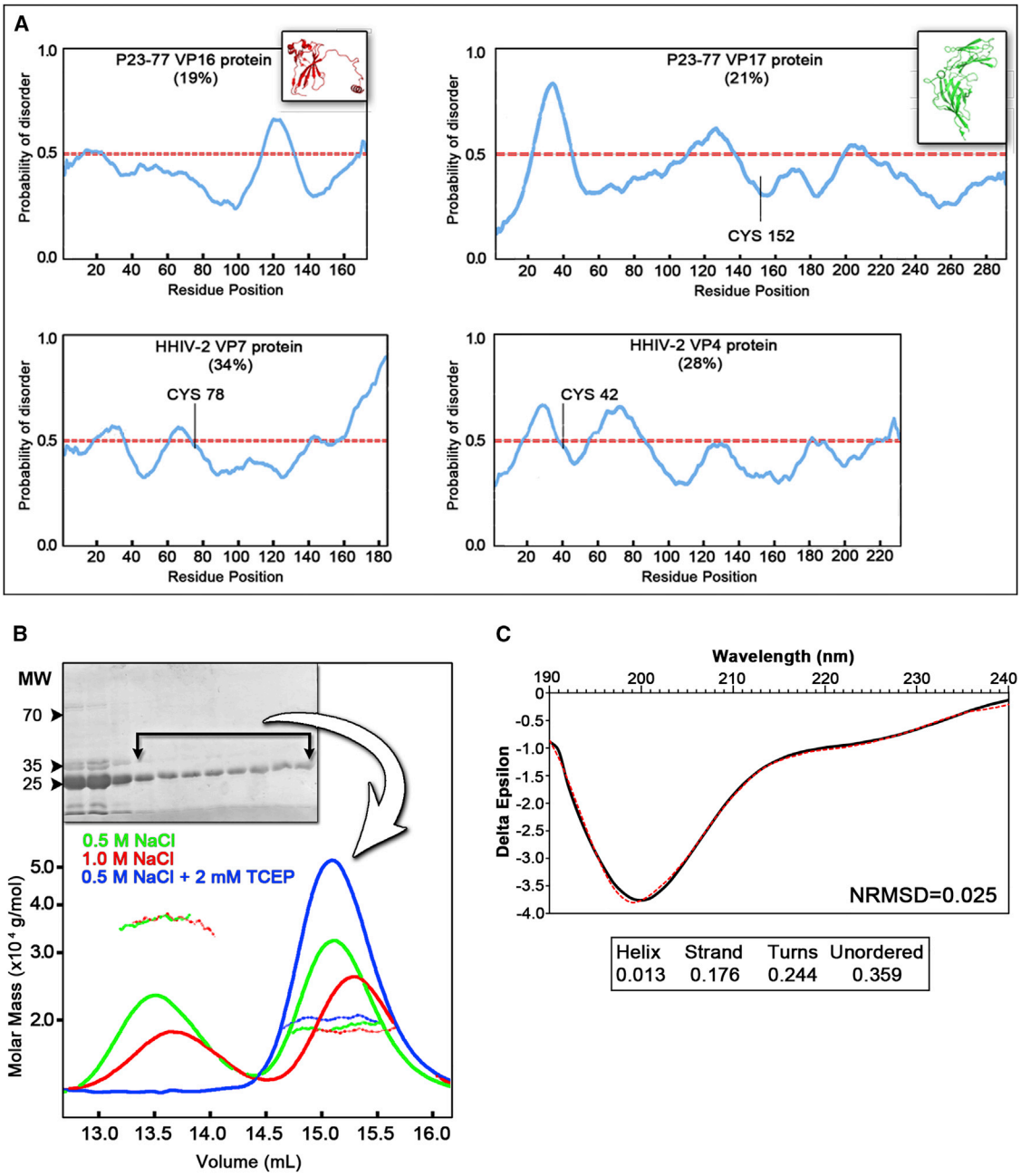

Figure 3. HHIV-2 MCPs VP4 and VP7

(A) Comparison of profiles of the probability of disorder per residue in corresponding MCPs of *Thermus* phage P23-77 (VP16 and VP17 represented as cartoon models in red and green, respectively; PDB: 3ZMN and 3ZMO) and archaeal virus HHIV-2 (VP7 and VP4) with cysteine residues marked. The total percentages of residues predicted to be disordered are in parentheses.

(B) Upper: Coomassie-stained SDS-PAGE gel of VP7 fractions after purifying by Ni-NTA chromatography (molecular weight [MW] in kDa). The fractions combined for the MALS experiment are indicated by the joined arrows. Lower: Molar mass distribution of VP7 in different buffer conditions as determined by MALS along the elution profile represented by the UV reading at 280 nm; peak at ~13.5 ml represents the VP7 dimer (green and red lines), peak at ~15.1 ml the monomeric VP7.

(C) VP7 CD spectrum (black line) with secondary structure assignment (below) and reconstructed data (red dashed line). NRMSD, normalized root-mean-square deviation.

See also Figure S3.

and ~22 Å (headgroup to headgroup) thick, respectively (Figures 4A and 4B). The icosahedral membrane encloses the linear dsDNA genome with an estimated density of ~370 mg/ml (Figure 4A). The DNA fills the entire volume of the membrane vesicle, as clearly shown by three peaks close to the inner membrane leaflet (Figure 4B, red arrows). The outer membrane leaflet

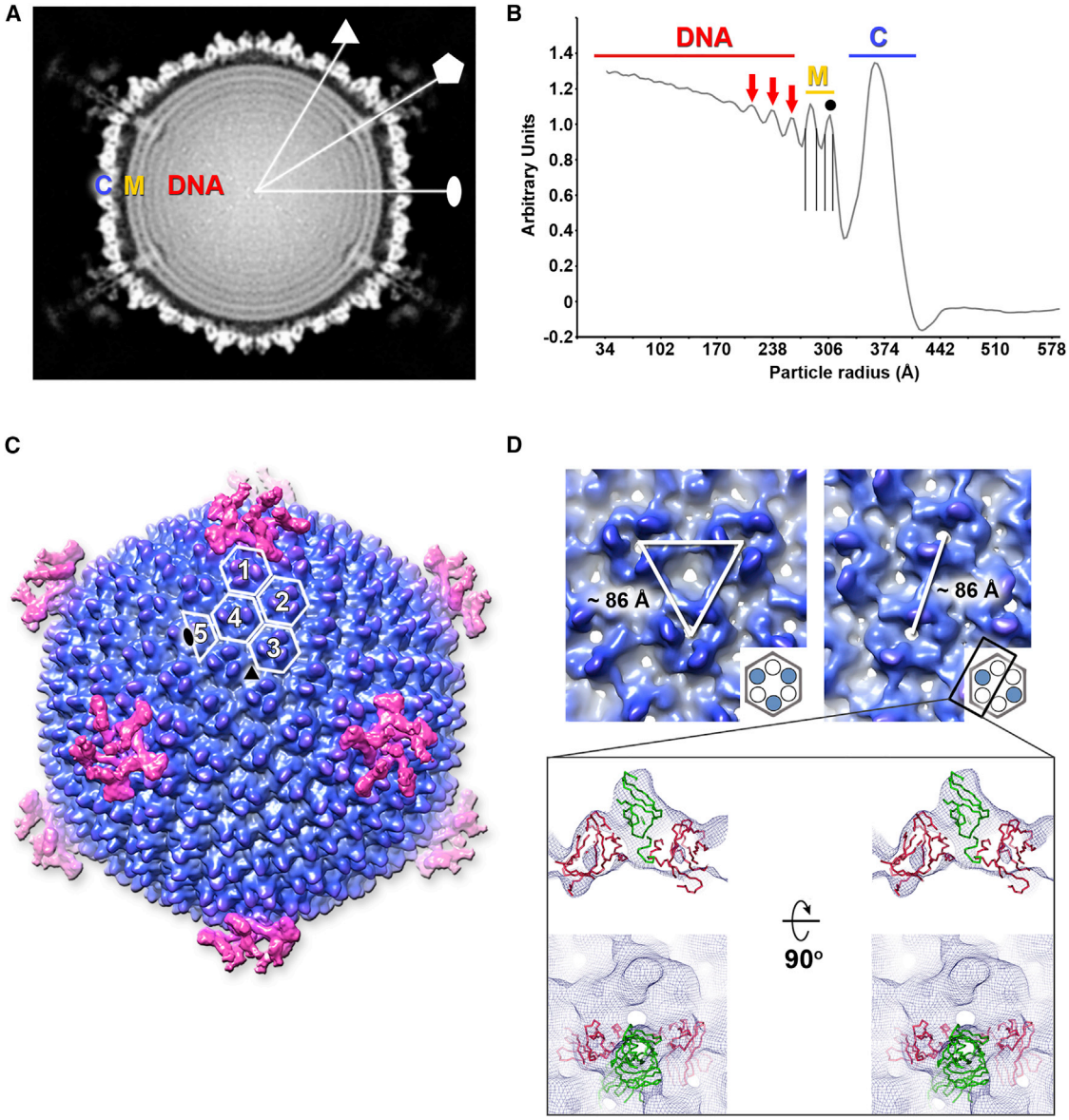

Figure 4. HHIV-2 Icosahedral Electron Density

(A) Central section of the 3D reconstructed electron density. The icosahedral symmetry axes (triangle, three-fold; pentagon, five-fold; oval, two-fold) and architectural elements (C, capsid; M, membrane; DNA, genome) are marked.

(B) Radial density profile of the 3D map with demarcation of the structural elements. The first three DNA layers are marked by the red arrows and the thinner outer membrane layer by the black dot.

(C) Overall view of the electron density of HHIV-2 contoured at 1σ (capsid, slate-blue; spike proteins at the five-fold vertices, light magenta). The hexagonal and half-hexagonal capsomers forming the icosahedral asymmetric unit are outlined in white. The two-turret capsomers are labeled 4 and 5. Capsomer 5 is located on the two-fold icosahedral symmetry axis (black oval). The three-turret capsomers are labeled 1–3. Capsomer 3 is proximal to the three-fold axis (black triangle).

(D) Electron density as solid surface (contoured at 2.5σ) of the three-turret capsomers (left) and two-turret capsomers (right). The distances between the centers of the capsomers are marked (left and right panels are not to scale). Schematic diagrams (bottom right) illustrate the organization of the pseudo-hexameric capsomers (white circles, VP7; slate-blue circles, VP4). The inset (below) shows the rigid body fitting of the P23-77 heterotrimer VP16-VP17-VP16 (VP16 and VP17 in red and green ribbons, respectively) into HHIV-2 density (as blue mesh contoured at 2.9σ). The inset is wall-eyed stereo view.

See also Figures S4 and S5.

is ~9 Å and the inner one ~12 Å thick, measured at mid-height of the corresponding peaks in the electron density profile (black vertical lines in Figure 4B).

Pentameric structures (~100 Å) protrude from the five-fold vertices (Figure 4C), which are plugged into the capsid shell by penton proteins (see below). The HHIV-2 icosahedral asymmetric unit is composed of five pseudo-hexagonal capsomers with two distinct morphologies (Figures 4C and 4D). One set of capsomers possesses three turrets (capsomers 1–3 in Figure 4C), while the other set bears two turrets (capsomers 4 and

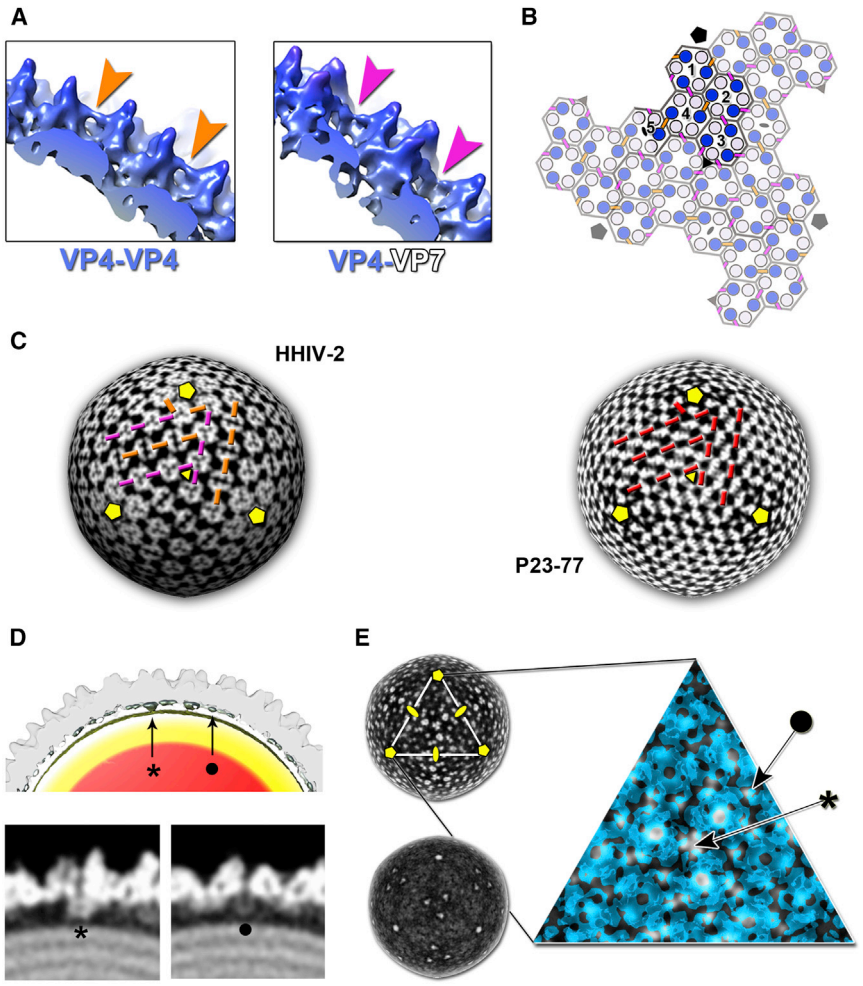

Figure 5. Capsomer Contacts

(A) HHIV-2 capsid density contoured at 3σ (blue). Left: Interaction between the two turret-bearing MCP densities (VP4-VP4; orange arrowheads). Right: Interaction between the turret-bearing and non-turret-bearing MCP densities (VP4-VP7; magenta arrowheads).

(B) Schematic representation of the icosahedral asymmetric unit of HHIV-2 (solid colors with numbers marking the capsomers 1–5 as in Figure 4C) with symmetry-related ones composing the virus facet (semi-transparent). The positions of VP4 and VP7 are marked by blue and blue-white circles. The intercapsomer contacts are labeled by bars color-coded as in (A). The icosahedral five-fold, three-fold, and two-fold axes are marked by black pentagons, triangles, and ovals, respectively.

(C) Side-by-side comparison of the icosahedral slices of HHIV-2 (left; at radius 400 Å) and phage P23-77 (right; at radius 392 Å) (protein is in white). Some of the corresponding bridging densities are marked and color-coded as in (A). For P23-77, the bridging density corresponding to the strand-swapping dimerization motif of the non-turret density of the vertical single β-barrel VP16 protein is marked by red bars. Yellow pentagons and triangles mark the icosahedral five- and three-fold symmetry axes; the two-fold axes have been omitted for clarity.

(D) Upper: Cut-through view of the HHIV-2 density map along the three-fold axis (capsid is in white for clarity; bridging density contoured at 0.8σ in gray; vesicle in yellow; genome in red). Lower left: Density along the plane bisecting the base of the capsomers around the three-fold icosahedral axis (capsomer 3, see B and Figure 4C). Lower right: As left, with the plane bisecting VP4 and VP7 MCPs. Stars and black circles mark the corresponding locations within the panels.

(E) Left: icosahedral slice of HHIV-2 at radius 355 Å (top) and radius 345 Å (below) showing the density underneath the capsid and approaching the membrane vesicle. White triangle marks the virus facet, and yellow pentagons and ovals label the icosahedral five- and two-fold symmetry axes, respectively (the three-fold axis has been omitted for clarity). The inset on the right shows the distribution of the density underneath the capsid (as semi-transparent blue, contoured at 3.4σ). Density is detected at the three-fold axis in correspondence to VP7 proteins (arrow with a star) and nearby (arrow with a black circle).

5 in Figure 4C). HHIV-2 virion structure displays a pseudo $T = 28$ *dextro* organization (the handedness was determined by cryo-ET as described in Figure S5A and the Supplemental Experimental Procedures). The estimated intercapsomer distance between the HHIV-2 pseudo-hexagonal capsomers is ~86 Å (Figure 4D).

Based on the capsid organization of P23-77 (Jaatinen et al., 2008; Rissanen et al., 2013), the density with the turret in HHIV-2 would correspond to MCP VP4. In this case, the three-turreted capsomer of HHIV-2 would be composed of alternating VP4 and VP7, VP7 representing the non-turreted β-barrel and analogous to P23-77 VP16 (Figure 4D, left). The two-turreted capsomer of HHIV-2 would then have two VP4 proteins (with turrets) and four VP7 monomers (Figure 4D, right and inset).

In HHIV-2 clear densities connect the MCPs at mid-height (Figure 5A). They connect either two MCPs with a turret, putative VP4-VP4 dimer (Figure 5A, left), or a turret-bearing MCP with an MCP without a turret, putative VP4-VP7 heterodimer (Figure 5A, right). These contacts bridge MCPs within and across the icosahedral asymmetric unit (Figure 5B, orange and magenta bars). In the P23-77 cryo-EM density map, an equivalent network of connecting densities is visible (Figure 5C). This corresponds to a strand-swapping dimerization motif in VP16-VP16 subunits (Rissanen et al., 2013). This observation strengthens the possibility that a putative homodimer VP4-VP4 and a heterodimer VP4-VP7 are also used as minimal building blocks for the HHIV-2 assembly. The similarity between the bridging densities of VP4-VP4 and VP4-VP7 (Figure 5A) might also indicate a shared mechanism for the homo- and heterodimerization of HHIV-2 MCPs. Moreover, ordered density beneath the HHIV-2 capsid is noticeably visible, although weaker when approaching the underlying membrane (Figures 5D and 5E, left). This appears to segregate toward the center of the virus facet, plugging the base of the capsomers around the three-fold axis (Figure 5E). In addition, density is detected at the three-fold axis in correspondence of VP7 proteins (Figure 5E, inset, arrow with a star) and nearby (Figure 5E inset, arrow with a black circle). At the five-fold vertices, a tubular density emerges from the vesicle (Figure 5E, bottom left).

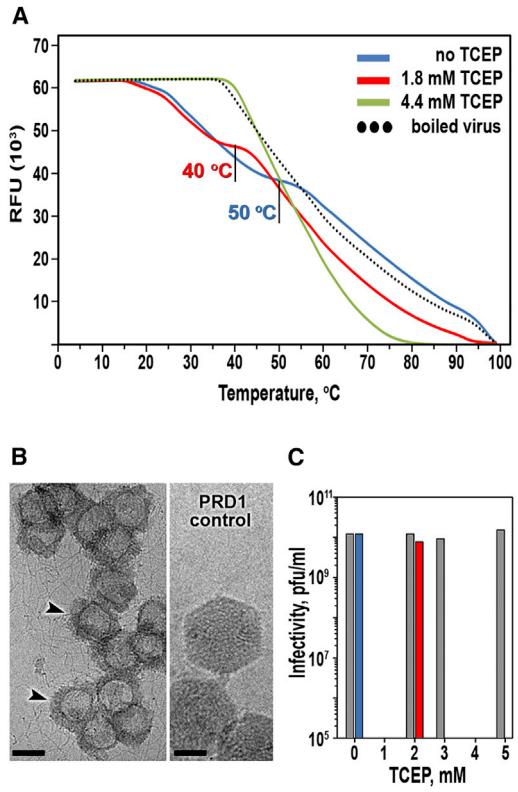

Figure 6. Virus Stability in Reducing Environment

(A) Monitoring the HHIV-2 genome release using SYT09 dye. Curves are colored according to the buffers (see the key). The dotted line corresponds to the virus sample boiled for 10 min at 75°C. The genome release temperatures T_r for the virus in the presence of increasing concentrations of TCEP are marked by a black line (incubation times: ~45 min for 1.8 mM TCEP and ~15 min for 4.4 mM TCEP). The first derivative of this plot is shown in Figure S6, top. RFU, relative fluorescence units.

(B) Left, 2D cryo-image of the virus in 4.4 mM TCEP used for (A), showing the virus morphological changes (black arrowheads). Scale bar, 50 nm. Right: 2D cryo-image of PRD1 in the same buffer conditions as HHIV-2 and used as a control, showing no detectable changes in the virus architecture (for the corresponding fluorescence spectra see Figure S6). Scale bar, 25 nm.

(C) Infectivities of PRD1 (gray bars; used for comparison) and HHIV-2 (bars color-coded as in A) were determined in the presence of TCEP after 3 hr of incubation at +5°C by plaque assay. Infectivity of HHIV-2 was below 10^5 plaque-forming units/ml with 3 and 5 mM TCEP.

See also Figure S6.

Reducing Environment Compromises HHIV-2 Stability and Infectivity

Thermostability plate-assay experiments for detection of genome release supported a decrease of the genome-releasing temperature (T_r) from 50° to 40°C in the presence of 1.8 mM TCEP reducing agent, and a more drastic effect with 4.4 mM TCEP (Figures 6A and S6). Cryo-imaging of the sample in 4.4 mM TCEP shows the loosening and removal of capsid proteins from the LC (Figure 6B, left). This effect was not observed in PRD1, which was used as a control (Figure 6B, right; Figure S6). Furthermore, HHIV-2 infectivity showed a clear decrease with increasing TCEP concentration (Figure 6C).

HHIV-2 Vertex Structure

The HHIV-2 vertex complex is composed of three structural elements: the penton, the "blade," and the fiber (Figure 7A and key). The penton is buried in the capsid (Figure 7A, bottom inset). The blade forms pentameric complexes that resemble five-blade propellers (Figure 7A, center inset). The third architectural element is the fiber (~150 Å long, ~25 Å diameter), which stems from the center of the vertex complex and is capped at the outermost end by density resembling a knob (Figure 7A, top inset). This density is weaker than the penton and blade densities, especially in the outermost region.

Underneath the vertex structure, a bullet-shaped density (~25 Å in height, ~25 Å in diameter) protrudes from the outer leaflet of the membrane, but its connectivity to the penton interior is weak. This density corresponds to a membrane-protein complex crossing the lipid bilayer (Figure 7A, key and bottom inset).

2D cryo-imaging of purified HHIV-2 displayed, among empty and DNA-filled viral membrane vesicles, viruses with a reduced number of spike complexes. To assess the architecture of these spikeless vertices, we performed cryo-ET on HHIV-2 with a lower number of spike complexes. By multi-reference classification and sub-tomogram averaging of individual vertices, sub-boxed from aligned 3D tomographic volumes of HHIV-2, we showed that the pentameric blades and fiber detach, leaving the penton within the capsid (Figure 7B, top). This analysis confirmed the presence of the fiber with a knob (Figure 7B, bottom). Segmentation of the spike components and analysis of corresponding volumes with a mass density of protein of 1.35 g/cm^3, in combination with dissociation studies (Figure 2B), allowed us to identify the proteins within the vertex complex. Based on this analysis, the penton would be composed of five copies of protein VP16 (27.8 kDa), structurally compatible with a single β-barrel protein and contacting radially with the peripentonal capsomers (Figure 7A, bottom inset). Also, the blade domain would correspond to a dimer of VP17 (43.3 kDa) (Figure 7A, center inset) whereas VP2 (51.4 kDa), which contains heptapeptide repeats typical of coiled-coil protein, could form the fiber as a trimeric molecule (Figure 7A, top inset).

DISCUSSION

Analysis of HHIV-2 MCPs Suggests a Vertical Single β-Barrel Fold

Comparison of the molecular masses and EM density morphologies of the turret and non-turret-bearing capsid subunits of the archaeal virus HHIV-2 and bacteriophage P23-77 indicates that HHIV-2 MCPs (VP4 and VP7) are counterparts of P23-77 MCPs (VP17 and VP16), despite the low (20%) sequence identities.

Disorder prediction analysis assigns a higher percentage of disordered residues for HHIV-2 MCPs than for P23-77 residues (Figure 3A). The first 40 residues of HHIV-2 VP4 share a common profile with corresponding amino acids of P23-77 VP17, of which residues 1–21 have been hypothesized to anchor the protein onto the virus membrane, with residues 22–42 forming a proline-rich helix preceding the β-barrel (Rissanen et al., 2013). By inference with this organization, the cysteine 42 in VP4 would be located at the base of the capsomers and might be available for disulfide bond formation (see below). The role of VP4 in the capsomer organization and its morphological similarities with

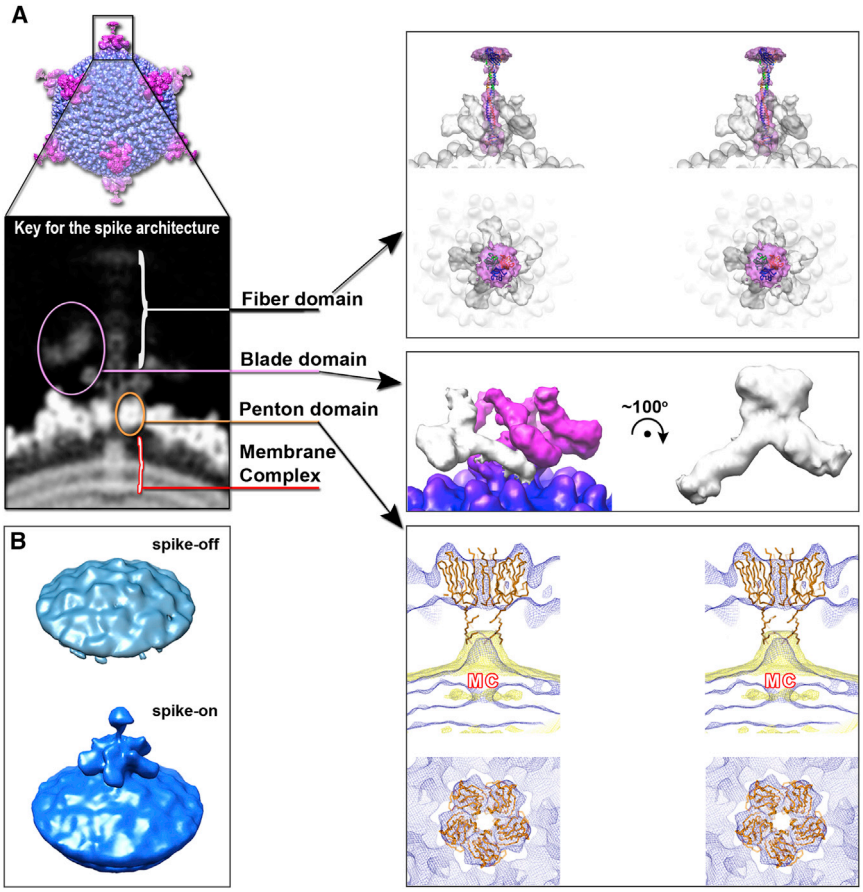

Figure 7. Architecture of the Vertex Complex

(A) Left: Overall view of HHIV-2 density contoured at low threshold (~0.06σ; capsid in slate-blue and spike complex in magenta) with below the central section of the electron density, corresponding to one of the vertices and serving as key for the components of the spike complex. Bottom inset: Density (slate-blue mesh) corresponding to the HHIV-2 penton domain contoured at 2.9σ and the vesicle underneath contoured at 2.0σ illustrated as wall-eyed stereo views (perpendicular to the five-fold icosahedral symmetry axis on top and along it on bottom); in yellow mesh, the density of the membrane vesicle contoured at lower threshold (1.0σ) with MC marking the membrane complex. Rigid body fitted into the penton density the atomic model of the STIV A223 penton base protein is shown as orange ribbon (Veesler et al., 2013). Center inset: Density corresponding to the pentameric blade domain shown as solid surface in light magenta (0.8σ) with one of the blades colored white. Top inset: fiber domain shown as stereo views as for the penton. The density of the fiber is in semi-transparent light magenta, and the rest of the virus is white. A chimeric model composed of the P22 tail needle gp26 (PDB: 2POH; Olia et al., 2007) and the atadenovirus fiber head domain (PDB: 4D1G; Singh et al., 2014) is manually fitted into the fiber density.

(B) Top: Sub-tomogram averaged class of vertices where the blade and fiber domains are absent but the penton is present (solid cyan, contoured at 2σ). Bottom: Sub-tomogram averaged class of virus vertices with complete spikes showing also the presence of the fiber domain (solid blue, contoured at 0.3σ). Both maps at ~21 Å at FSC = 0.143. See also Figure S5.

P23-77 VP17 points to a protein with a single vertical β-barrel fold (Figure 4D). Non-turret-bearing HHIV-2 VP7 subunit is predicted to be almost 50% more disordered than its P23-77 counterpart, VP16 (Figure 3A, left). However, considering the HHIV-2 VP7 secondary structure CD assignment and the morphological similarity between capsomers in P23-77 and HHIV-2, we propose that the VP7 core also possesses one vertical single β-barrel but with flexible terminal ends. In solution, recombinant VP7 molecules exist as both monomers and dimers, the latter formed by an intermolecular disulfide bond via cysteine 78 (Figure 3B).

Disulfide Bonds: Molecular Locks in HHIV-2 Virion Capsid Assembly

Thermostability and plaque assays with 2D cryo-imaging of HHIV-2 show that a reducing environment compromises the capsid stability and virus infectivity (Figure 6). These results strongly support that the formation of disulfide bonds across HHIV-2 MCPs is a pivotal capsid stabilization mechanism in the virus assembly pathway.

In contrast to P23-77 VP16 protein, which forms a stable homodimer in solution (Rissanen et al., 2013), HHIV-2 VP7 in non-reducing conditions exists as monomers and dimers, and the intermolecular disulfide bridging is the only way of forming stable homodimers in solution. The VP7 monomeric state indicates that the cysteine 78 residue might not always be available for disulfide bonding as a consequence of the residue being in a disorder-prone region (Figure 3A, left). The ability of VP7 to form dimers via an S-S bridge in vitro might be tuned in vivo by the interaction with VP4, by its final location within the virus facet, and/or by other viral proteins. One of the first 50 residues of VP4 is a cysteine juxtaposed to a disordered region (Figure 3A, right). Thus, inter- and/or intramolecular disulfide bonds could assist the functional capsomer assembly. All of these cysteines are conserved in the MCPs of SH1 and PH1 viruses (Porter et al., 2013). Haloarchaeal viruses that use disulfide bridging for capsid stabilization, such as HHIV-2 (and possibly SH1 and PH1), must have a mechanism for favoring disulfide bond formation inside the cell, despite *Haloarcula hispanica* reducing intracellular conditions (Srivastava and Kowshik, 2013).

HHIV-2 Capsid Organization in Light of the Structure-Based Virus Lineages

The HHIV-2 capsomers show two- and three-turret morphologies similar to those of SH1, but different from the two-turret capsomer morphology in P23-77, whereas the triangulation number (pseudo $T = 28$ *dextro*) and capsomer footprint are conserved in all three (Figure 8A).

The discovery of vertical single β-barrels in the P23-77 MCPs VP16 and VP17 led to the proposal of a vertical β-barrel viral superlineage whose suggested hierarchy is based on the

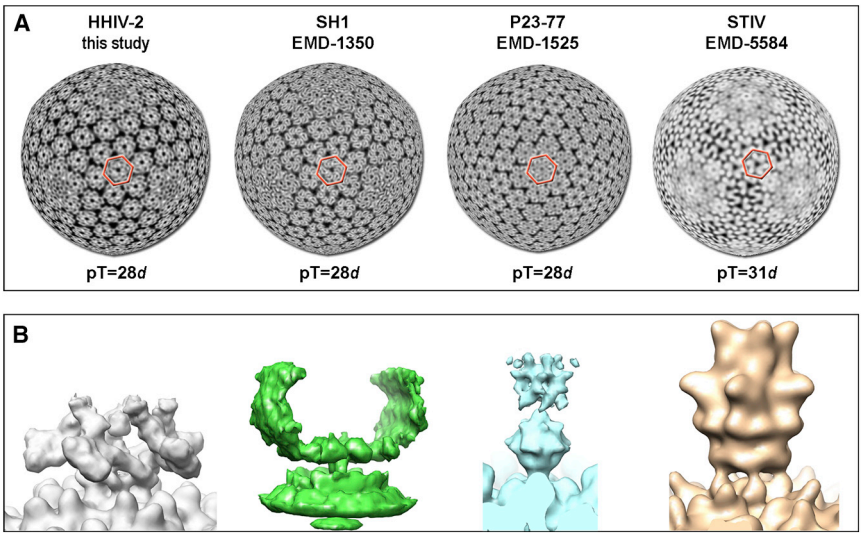

Figure 8. Splitting of the Conserved and Evolving Structural Elements in the Virion Architecture

(A) Radial cross sections at the base of the capsomers in HHIV-2, SH1, P23-77, and STIV viruses showing the conservation of the capsomer pseudo-hexameric footprint (red hexagon marks one capsomer base) across viruses with vertical single β-barrel MCPs (HHIV-2, SH1, and P23-77). STIV as representative of the PRD1 adenoviral lineage with one double β-barrel MCP is shown for comparison.

(B) Different architectures of the spike complexes responsible for host cell recognition and attachment. From left to right: HHIV-2, SH1 (EMD: EMD-1498), P23-77 (EMD: EMD-1525), and STIV (EMD: EMD-5584) undecorated particles as the spikes lack the petal-like structures (Veesler et al., 2013). The individual panels in (A) and (B) are not to scale.

topological differences between the β-barrels in P23-77 and those in double β-barrel viruses (Rissanen et al., 2013). However, the pseudo-hexameric footprint in the lattice-forming building blocks is the conserved structural feature in both of these virus types (Figures 1 and 8A), although the intercapsomer distance for single β-barrel viruses is larger (~86 Å) than in the double β-barrel viruses (~75 Å) (Abrescia et al., 2004, 2008; Hyun et al., 2011; Khayat et al., 2005; Yan et al., 2009). The conservation of the pseudo-hexameric footprint of the lattice-forming capsomer base is in contrast with the remarkable structural variability of the spike complexes responsible for virus cell recognition and attachment (Figure 8B). While HHIV-2 and SH1 infect *Har. hispanica*, their five-fold vertices have completely different structures (Figure 8). The HHIV-2 vertex complex contains a propeller-like structure and a flexible fiber stemming from the center, which we tentatively attribute to VP17 and VP2, respectively. Interestingly, HHIV-2 VP2 protein has internal sequence repeats (as SH1 VP2) (Jaakkola et al., 2012) that, together with the corresponding protein electron density, is reminiscent of the gp26 fiber of bacteriophage P22 (Olia et al., 2007) (Figure 7A, top inset). The blade domain of the HHIV-2 vertex complex interacts with the penton protein (putative VP16). The penton acts as a "converter plug," capable of hosting different spike proteins and interlocking with the membrane proteins. This type of internal interaction has been visualized only for the archaeal virus STIV (Veesler et al., 2013), but may also be present in P23-77. The membrane-protein complex plugging the icosahedral vertices of the membrane vesicle (Figure 7A, key and bottom inset) is a clear common structural element in euryarchaeal HHIV-2 and SH1, crenarchaeal STIV, and thermophilic phage P23-77. Despite the apparent structural diversity in the outer vertex complex domains of these viruses (Figure 8B), the HHIV-2 spike complex architecture highlights a common mechanism in the modular assembly of the vertex subunits from the membrane to the spike.

Assembly of Internal Membrane-Containing Icosahedral Viruses with Two Vertical Single β-Barrel MCP Species

A mechanism for the capsid assembly of P23-77 was recently outlined based on the crystal structures of the MCPs VP17 and VP16 fitted into a ~14-Å resolution virus density map (Rissanen et al., 2013). It was also suggested to apply to the archaeal virus SH1. In P23-77, VP16-VP16 homodimers form via strand-swapping interaction and act as binding platforms for single VP17 molecules. The VP16-VP16 strand swapping is seen as bridging densities between capsomers in the P23-77 virus density map (Jaatinen et al., 2008; Rissanen et al., 2013). A similar pattern of contacts is distinguishable in HHIV-2 (Figures 5A–5C) but there are two types of bridges (Figure 5A), which would correspond to VP4-VP4 homodimers and VP4-VP7 heterodimers.

This implies that: (1) VP4 is capable of switching its interacting partner, and (2) the building blocks used for assembly are VP4-VP4 and VP4-VP7. Disulfide bonding between MCPs and/or other viral proteins might be used to stabilize the capsid shell. Thus, whereas the MCP dimerization is an obligatory step in the assembly of vertical single β-barrel viruses, the dimerization mechanism might be virus specific provided that the single vertical β-barrels fulfill the formation of a closely packed *P*3 lattice (Figure 9A). But how do the dimeric building blocks organize into capsomers with pseudo-hexameric footprint? The density connecting the HHIV-2 capsid to the LC provides some clues about the assembly (Figures 5D and 5E). The membrane-bound protein complex at the five-fold vertices (Figure 7A, key and bottom inset), and/or the density cross-talking between the capsid and the LC, particularly evident at the icosahedral three-fold axis and at the center of the capsomers around the three-fold axis (Figures 5D and 5E), could co-direct the organization of the MCPs onto the virus facet. Evidence of such a guiding principle is the use of VP4-VP4 dimers around the five-fold and VP4-VP7 dimers at the three-fold axis, although both the peripentonal and the three-fold capsomers display the same three-turret morphology (Figures 5B and 5C). For example, in bacteriophage PM2 a network of two major transmembrane proteins offers a platform for the correct registering of pseudo-hexameric capsomers (Abrescia et al., 2008). Thus, for the vertical single β-barrel viruses, the interaction between the capsid and the membrane might be an indispensable "global positioning system" as manifested by icosahedrally ordered densities approaching the membrane vesicle (Figures 5E, 9A, left and 9B, left). In

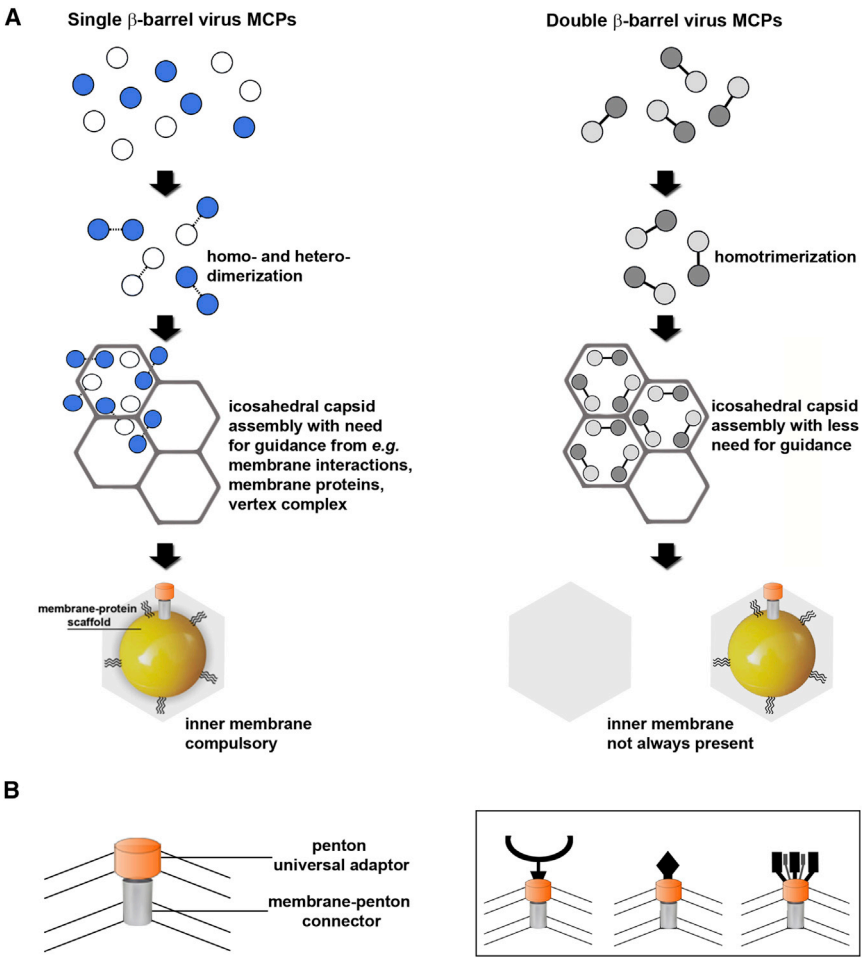

Figure 9. Model for Assembly of Vertical Single and Double β-Barrel Viruses and Deconvolution of Capsid from Receptor Binding Proteins

(A) Left: For vertical single β-barrel MCPs (blue, white circles; see also Figure 1B), the formation of a double β-barrel complex requires dimerization mechanisms, which may be virus or environmental specific. Correct pseudo-hexameric capsomer formation and registering onto the virus vesicle (depicted as a yellow sphere) may strongly rely on assembly nucleation signals or guiding proteins as membrane-associated proteins at the five-fold and/or proximal to the three-fold icosahedral axes. Right: For double β-barrel MCPs (dark gray, gray circles; see also Figure 1A), the pseudo-hexameric capsomers are readily formed by the homotrimerization, leaving only the rotational registering of capsomers to adjust for correct assembly.

(B) A schematic model of the five-fold vertex complex. The penton universal adaptor and membrane-penton connector are conserved parts of the vertex structure, and the host-interacting spike (gallery shown on right) is an exchangeable unit.

addition, membrane scaffolding proteins could assist this process, possibly by "sizing" the membrane vesicle. Vertical double β-barrel viruses, such as adenovirus, can assemble without a protein-membrane guiding system (Figure 9A, right), although scaffolding proteins might also be required (Roberts et al., 1986). In the case of PRD1, it has been demonstrated that virus-encoded non-structural scaffolding membrane protein P10 is utilized in the particle assembly (Rydman et al., 2001). As the capsid assembly of the vertical single β-barrel viruses is considered to be more complex than that of the vertical double β-barrel viruses, it is most conceivable that such viruses also have a scaffolding machinery to organize the viral lattice.

In conclusion, emerging knowledge on tailless icosahedral internal membrane-containing viruses with vertical single β-barrel MCPs suggests that the increased degree of freedom for homo- and heterodimerization of the MCPs requires additional molecular guidance for successful virus assembly (Figure 9). We propose that this process relies on two general principles: (1) the vertical single β-barrel MCPs have evolved with specific dimerization mechanisms; (2) the network of interactions connecting the capsomers and the membrane vesicle via direct MCP contacts or via membrane-associated proteins drives the nucleation for the correct assembly. In this light, the host-recognizing vertex proteins (Figure 9B, right) remain interchangeable accessories to the assembly, only obeying environmental evolutionary pressure.

EXPERIMENTAL PROCEDURES

Virus Production and Purification

HHIV-2 was grown on *Har. hispanica* (ATCC 33960) (Jaakkola et al., 2012). HHIV-2 production was carried out using modified growth medium containing 5 g of peptone and 1 g of Bacto yeast extract per liter (Nuttall and Dyall-Smith, 1993). 30% (w/v) artificial salt water (Dyall-Smith, 2009) was added to top-layer agar, plates, and liquid medium to give the final concentrations of 18%, 20%, and 23% (w/v), respectively. For HHIV-2 purification, see the Supplemental Experimental Procedures. PRD1 production and purification has been described elsewhere (Bamford and Bamford, 1991).

Dissociation of Viral Particles

Purified HHIV-2 particles (1 mg/ml) were exposed to various conditions (see Table S1). Protease treatments included incubation in proteinase K (0.1 mg/ml; Roche), trypsin (0.1 mg/ml; Sigma), or bromelain (7.0 mg/ml; ICN Biomedicals) for 2 hr at 37°C. Temperature treatments used were freezing (−20°C) and thawing, incubation at 70°C for 30 min, or at 37°C for 24 or 48 hr. Different buffer conditions and chaotropic agents, including guanidine hydrochloride and urea, were also tested (see the Supplemental Experimental Procedures).

Lipid Extraction and Analysis

Lipids were extracted from *Har. hispanica* cells (stationary growth phase), and 2× purified HHIV-2, as previously described (Folch et al., 1957) and detailed in the Supplemental Experimental Procedures.

VP7 Expression and Purification

HHIV-2 gene *24* encoding VP7 (Uniprot: H9AZX1) was cloned into pOPIN-E plasmid (with C-terminal HisTag) (Berrow et al., 2007). Protein expression was carried out in *Escherichia coli* Rosetta BL21 (DE3) pLysS cells induced with 1 mM isopropyl β-D-1-thiogalactopyranoside. Growth was continued overnight at 20°C. The cells were harvested by centrifugation and resuspended in buffer with 50 mM Tris-HCl (pH 7.5), 0.5 M NaCl, and 2 mM β-mercaptoethanol

(β-ME), followed by the addition of EDTA-free protease inhibitors (Roche) and DNase I (4 μg/ml; Fermentas) for subsequent protein extraction and purification (details in the Supplemental Experimental Procedures).

Circular Dichroism

For CD experiments, recombinant VP7 was diluted into 20 mM potassium phosphate (pH 7.4) with 150 mM NaCl, and the same with 1 mM β-ME. For each sample the final concentration was assessed by Nanodrop spectrophotometer at 280 nm by averaging three consecutive measurements. CD spectra measured at 21°C were repeated five times and averaged with the baseline subtracted on a Jasco series J-815 spectropolarimeter. Hellma-absorption cell (type QS) with a path light length of 0.1 mm was used to obtain spectral data in the 190–260 nm region. Data were analyzed using the DICHROWEB server (Whitmore and Wallace, 2008) (Supplemental Experimental Procedures).

HHIV-2 Thermostability and Infectivity Assays

Thermal stability assays using HHIV-2 and PRD1 were performed by adapting previously described protocols (Walter et al., 2012). For these experiments, SYTO9 (5 mM stock; S-34854, Molecular Probes/Life Technologies) dye was used to detect the release of nucleic acids. The Bio-Rad CFX96 real-time PCR detection system was used for fluorescence readout of samples dispensed (50 μl) in 96-well plates (Thermo-Fisher). The experiment consisted of elevating the temperature from 4° to 99°C and taking the fluorescence reading every 0.5°C after holding for 10 s. Each buffer condition was assayed four times, using 200 μl of premixed stock solution. Details on buffer conditions used and the protocol for the infectivity assay can be found in the Supplemental Experimental Procedures.

HHIV-2 Cryo-EM and Cryo-ET

For 2D cryo-imaging, 4 μl of HHIV-2 (0.9–1.2 mg/ml) in HHIV-2 buffer were pipetted onto 200-mesh Quantifoil R 2/1 holey-carbon grids and vitrified using a Vitrobot (FEI). Images were acquired with a JEM-2200FS/CR (JEOL Ltd.) electron microscope, operating at 200 kV at liquid nitrogen temperature, at a defocus range from 0.7 to 3.0 μm with a dose of ~20 $e^-/Å^2$. A total of 891 images were manually recorded with a 4K × 4K Ultrascan 4000 CCD camera (Gatan) at a nominal magnification of 60,000×, producing a final pixel size of 1.7 Å. An in-column omega energy filter was used with the energy slit width set at 12 eV. During pre-processing the images were binned, and a total of 4,875 particles (underfocus range 0.7–2.7 μm) contributed to the final 3D icosahedral reconstruction obtained by iterative projection matching by XMIPP 3.0 (Scheres et al., 2008) with angular sampling up to 0.2°. As initial reference a cryo-ET reconstruction of HHIV-2 filtered to 80 Å was used (Figures S5A and S5B). The resolution of the final map estimated by FSC using the 0.5 criterion for the capsid (a soft mask was used between 340 and 425 Å radius) was 13.0 Å (Figure S4). A negative temperature factor of 1,000 $Å^2$ was applied to the final reconstruction. Cryo-ET and sub-tomogram averaging procedures are described in the Supplemental Experimental Procedures.

Sequence and Structure Analysis

Disorder prediction was carried out using RONN v3.2 (Yang et al., 2005), and the analysis of the reconstructed virus and LCs was carried out using CHIMERA (Pettersen et al., 2004), *Dynamo* (Castaño-Díez et al., 2012), and Amira (Visage Imaging) software. For details of model fitting and further analysis, see the Supplemental Experimental Procedures.

ACCESSION NUMBERS

The HHIV-2 cryo-EM reconstruction has been deposited in the EMDataBank with the accession code EMD-3109, and the cryo-ET sub-tomogram averaged density for the vertices with spike on/off with accession codes EMD-3110 and EMD-3111, respectively.

SUPPLEMENTAL INFORMATION

Supplemental Information includes Supplemental Experimental Procedures, six figures, and one table and can be found with this article online at http://dx.doi.org/10.1016/j.str.2015.07.015.

AUTHOR CONTRIBUTIONS

H.M.O., D.H.B., and N.G.A.A. conceived the study. S.T.J. and H.M.O. produced the virus, and performed dissociation and lipid studies. D.G.C., B.P., and N.G.A.A. collected EM data and processed images. D.G.C., D. C-D., and N.G.A.A. collected ET data, and performed tomographic processing and sub-tomogram averaging. D.C. and N.G.A.A. produced and purified VP7 protein and performed biophysical experiments. All authors critically contributed to the analysis and interpretation of the data. H.M.O., D.H.B., and N.G.A.A. wrote the paper with contributions from the rest of the authors.

ACKNOWLEDGMENTS

We thank Marina Ondiviela for valuable assistance in VP7 protein production and purification, Sandra Delgado and Daniel Badia-Martinez, respectively, for help in virus imaging and image processing and analysis. Sari Korhonen, Soile Storman, and Isaac Santos Pérez are thanked for skillful support in virus production and infectivity assays, and Maider Villate, Eva Cunha, and the Genomic Platform at the CIC bioGUNE for assistance on MALS, CD, and thermofluor experiments, respectively. We are grateful to Ilona Rissanen and David I. Stuart for providing the coordinates of the icosahedral asymmetric unit of VP16 and VP17 fitted into the P23-77 electron density. We are also thankful to the OPPF (Oxford) for the pOPIN suite, and the Direction of the Salina of the Margherita di Savoia (Foggia, Italy) for the visit to the salt-pan from where HHIV-2 was isolated. This study was supported by Academy Professor (Academy of Finland) grants 255342, 256518, and 283072 (to D.H.B.), and the Spanish Ministerio de Economía y Competitividad (BFU2012-33947 to N.G.A.A). We thank Academy of Finland (grants 271413 and 272853) and the University of Helsinki for the support given to the EU ESFRI Instruct Centre for Virus Production (ICVIR) used in this study. Isaac Santos Pérez internship at the ICVIR was supported by Instruct.

Received: May 6, 2015
Revised: July 29, 2015
Accepted: July 29, 2015
Published: August 27, 2015

REFERENCES

Aalto, A.P., Bitto, D., Ravantti, J.J., Bamford, D.H., Huiskonen, J.T., and Oksanen, H.M. (2012). Snapshot of virus evolution in hypersaline environments from the characterization of a membrane-containing Salisaeta icosahedral phage 1. Proc. Natl. Acad. Sci. USA *109*, 7079–7084.

Abrescia, N.G., Cockburn, J.J., Grimes, J.M., Sutton, G.C., Diprose, J.M., Butcher, S.J., Fuller, S.D., San Martin, C., Burnett, R.M., Stuart, D.I., et al. (2004). Insights into assembly from structural analysis of bacteriophage PRD1. Nature *432*, 68–74.

Abrescia, N.G., Grimes, J.M., Kivelä, H.M., Assenberg, R., Sutton, G.C., Butcher, S.J., Bamford, J.K., Bamford, D.H., and Stuart, D.I. (2008). Insights into virus evolution and membrane biogenesis from the structure of the marine lipid-containing bacteriophage PM2. Mol. Cell *31*, 749–761.

Abrescia, N.G., Bamford, D.H., Grimes, J.M., and Stuart, D.I. (2012). Structure unifies the viral universe. Annu. Rev. Biochem. *81*, 795–822.

Bamford, J.K., and Bamford, D.H. (1991). Large-scale purification of membrane-containing bacteriophage PRD1 and its subviral particles. Virology *181*, 348–352.

Bamford, D.H., Grimes, J.M., and Stuart, D.I. (2005a). What does structure tell us about virus evolution? Curr. Opin. Struct. Biol. *15*, 655–663.

Bamford, D.H., Ravantti, J.J., Rönnholm, G., Laurinavicius, S., Kukkaro, P., Dyall-Smith, M., Somerharju, P., Kalkkinen, N., and Bamford, J.K. (2005b). Constituents of SH1, a novel lipid-containing virus infecting the halophilic euryarchaeon Haloarcula hispanica. J. Virol. *79*, 9097–9107.

Benson, S.D., Bamford, J.K., Bamford, D.H., and Burnett, R.M. (1999). Viral evolution revealed by bacteriophage PRD1 and human adenovirus coat protein structures. Cell *98*, 825–833.

Berrow, N.S., Alderton, D., Sainsbury, S., Nettleship, J., Assenberg, R., Rahman, N., Stuart, D.I., and Owens, R.J. (2007). A versatile ligation-independent cloning method suitable for high-throughput expression screening applications. Nucleic Acids Res. *35*, e45.

Castaño-Díez, D., Kudryashev, M., Arheit, M., and Stahlberg, H. (2012). Dynamo: a flexible, user-friendly development tool for subtomogram averaging of cryo-EM data in high-performance computing environments. J. Struct. Biol. *178*, 139–151.

Dyall-Smith, M. (2009). Halohandbook (M. Dyall-Smyth). http://www.haloarchaea.com/resources/halohandbook/.

Folch, J., Lees, M., and Sloane Stanley, G.H. (1957). A simple method for the isolation and purification of total lipids from animal tissues. J. Biol. Chem. *226*, 497–509.

Grimes, J.M., Burroughs, J.N., Gouet, P., Diprose, J.M., Malby, R., Ziéntara, S., Mertens, P.P., and Stuart, D.I. (1998). The atomic structure of the bluetongue virus core. Nature *395*, 470–478.

Happonen, L.J., Redder, P., Peng, X., Reigstad, L.J., Prangishvili, D., and Butcher, S.J. (2010). Familial relationships in hyperthermo- and acidophilic archaeal viruses. J. Virol. *84*, 4747–4754.

Hogle, J.M., Chow, M., and Filman, D.J. (1985). Three-dimensional structure of poliovirus at 2.9 Å resolution. Science *229*, 1358–1365.

Hong, C., Oksanen, H.M., Liu, X., Jakana, J., Bamford, D.H., and Chiu, W. (2014). A structural model of the genome packaging process in a membrane-containing double stranded DNA virus. PLoS Biol. *12*, e1002024.

Hyun, J.K., Accurso, C., Hijnen, M., Schult, P., Pettikiriarachchi, A., Mitra, A.K., and Coulibaly, F. (2011). Membrane remodeling by the double-barrel scaffolding protein of poxvirus. PLoS Pathog. *7*, e1002239.

Jaakkola, S.T., Penttinen, R.K., Vilen, S.T., Jalasvuori, M., Rönnholm, G., Bamford, J.K., Bamford, D.H., and Oksanen, H.M. (2012). Closely related archaeal *Haloarcula hispanica* icosahedral viruses HHIV-2 and SH1 have nonhomologous genes encoding host recognition functions. J. Virol. *86*, 4734–4742.

Jäälinoja, H.T., Roine, E., Laurinmäki, P., Kivelä, H.M., Bamford, D.H., and Butcher, S.J. (2008). Structure and host-cell interaction of SH1, a membrane-containing, halophilic euryarchaeal virus. Proc. Natl. Acad. Sci. USA *105*, 8008–8013.

Jaatinen, S.T., Happonen, L.J., Laurinmäki, P., Butcher, S.J., and Bamford, D.H. (2008). Biochemical and structural characterisation of membrane-containing icosahedral dsDNA bacteriophages infecting thermophilic *Thermus thermophilus*. Virology *379*, 10–19.

Khayat, R., Tang, L., Larson, E.T., Lawrence, C.M., Young, M., and Johnson, J.E. (2005). Structure of an archaeal virus capsid protein reveals a common ancestry to eukaryotic and bacterial viruses. Proc. Natl. Acad. Sci. USA *102*, 18944–18949.

Kivelä, H.M., Roine, E., Kukkaro, P., Laurinavicius, S., Somerharju, P., and Bamford, D.H. (2006). Quantitative dissociation of archaeal virus SH1 reveals distinct capsid proteins and a lipid core. Virology *356*, 4–11.

Laurinavicius, S., Käkelä, R., Somerharju, P., and Bamford, D.H. (2004). Phospholipid molecular species profiles of tectiviruses infecting Gram-negative and Gram-positive hosts. Virology *322*, 328–336.

Nuttall, S.D., and Dyall-Smith, M.L. (1993). Ch2, a novel halophilic archaeon from an Australian solar saltern. Int. J. Syst. Bacteriol. *43*, 729–734.

Olia, A.S., Casjens, S., and Cingolani, G. (2007). Structure of phage P22 cell envelope-penetrating needle. Nat. Struct. Mol. Biol. *14*, 1221–1226.

Peralta, B., Gil-Carton, D., Castaño-Díez, D., Bertin, A., Boulogne, C., Oksanen, H.M., Bamford, D.H., and Abrescia, N.G. (2013). Mechanism of membranous tunnelling nanotube formation in viral genome delivery. PLoS Biol. *11*, e1001667.

Pettersen, E.F., Goddard, T.D., Huang, C.C., Couch, G.S., Greenblatt, D.M., Meng, E.C., and Ferrin, T.E. (2004). UCSF Chimera—a visualization system for exploratory research and analysis. J. Comput. Chem. *25*, 1605–1612.

Pietilä, M.K., Laurinmäki, P., Russell, D.A., Ko, C.C., Jacobs-Sera, D., Hendrix, R.W., Bamford, D.H., and Butcher, S.J. (2013). Structure of the archaeal head-tailed virus HSTV-1 completes the HK97 fold story. Proc. Natl. Acad. Sci. USA *110*, 10604–10609.

Porter, K., Kukkaro, P., Bamford, J.K., Bath, C., Kivelä, H.M., Dyall-Smith, M.L., and Bamford, D.H. (2005). SH1: a novel, spherical halovirus isolated from an Australian hypersaline lake. Virology *335*, 22–33.

Porter, K., Tang, S.-L., Chen, C.-P., Chiang, P.-W., Hong, M.-J., and Dyall-Smith, M. (2013). PH1: an archaeovirus of *Haloarcula hispanica* related to SH1 and HHIV-2. Archaea *2013*, 456318.

Reinisch, K.M., Nibert, M.L., and Harrison, S.C. (2000). Structure of the reovirus core at 3.6 Å resolution. Nature *404*, 960–967.

Rissanen, I., Grimes, J.M., Pawlowski, A., Mäntynen, S., Harlos, K., Bamford, J.K., and Stuart, D.I. (2013). Bacteriophage P23-77 capsid protein structures reveal the archetype of an ancient branch from a major virus lineage. Structure *21*, 718–726.

Roberts, M.M., White, J.L., Grutter, M.G., and Burnett, R.M. (1986). Three-dimensional structure of the adenovirus major coat protein hexon. Science *232*, 1148–1151.

Rossmann, M.G., Arnold, E., Erickson, J.W., Frankenberger, E.A., Griffith, J.P., Hecht, H.J., Johnson, J.E., Kamer, G., Luo, M., Mosser, A.G., et al. (1985). Structure of a human common cold virus and functional relationship to other picornaviruses. Nature *317*, 145–153.

Rydman, P.S., Bamford, J.K., and Bamford, D.H. (2001). A minor capsid protein P30 is essential for bacteriophage PRD1 capsid assembly. J. Mol. Biol. *313*, 785–795.

Scheres, S.H., Nunez-Ramirez, R., Sorzano, C.O., Carazo, J.M., and Marabini, R. (2008). Image processing for electron microscopy single-particle analysis using XMIPP. Nat. Protoc. *3*, 977–990.

Singh, A.K., Menendez-Conejero, R., San Martin, C., and van Raaij, M.J. (2014). Crystal structure of the fibre head domain of the atadenovirus snake adenovirus 1. PLoS One *9*, e114373.

Srivastava, P., and Kowshik, M. (2013). Mechanisms of metal resistance and homeostasis in haloarchaea. Archaea *2013*, 732864.

Strömsten, N.J., Bamford, D.H., and Bamford, J.K. (2005). In vitro DNA packaging of PRD1: a common mechanism for internal-membrane viruses. J. Mol. Biol. *348*, 617–629.

Veesler, D., and Cambillau, C. (2011). A common evolutionary origin for tailed-bacteriophage functional modules and bacterial machineries. Microbiol. Mol. Biol. Rev. *75*, 423–433.

Veesler, D., Ng, T.S., Sendamarai, A.K., Eilers, B.J., Lawrence, C.M., Lok, S.M., Young, M.J., Johnson, J.E., and Fu, C.Y. (2013). Atomic structure of the 75 MDa extremophile *Sulfolobus* turreted icosahedral virus determined by CryoEM and X-ray crystallography. Proc. Natl. Acad. Sci. USA *110*, 5504–5509.

Walter, T.S., Ren, J., Tuthill, T.J., Rowlands, D.J., Stuart, D.I., and Fry, E.E. (2012). A plate-based high-throughput assay for virus stability and vaccine formulation. J. Virol. Methods *185*, 166–170.

Whitmore, L., and Wallace, B.A. (2008). Protein secondary structure analyses from circular dichroism spectroscopy: methods and reference databases. Biopolymers *89*, 392–400.

Yan, X., Yu, Z., Zhang, P., Battisti, A.J., Holdaway, H.A., Chipman, P.R., Bajaj, C., Bergoin, M., Rossmann, M.G., and Baker, T.S. (2009). The capsid proteins of a large, icosahedral dsDNA virus. J. Mol. Biol. *385*, 1287–1299.

Yang, Z.R., Thomson, R., McNeil, P., and Esnouf, R.M. (2005). RONN: the bio-basis function neural network technique applied to the detection of natively disordered regions in proteins. Bioinformatics *21*, 3369–3376.

Zhang, Z., Liu, Y., Wang, S., Yang, D., Cheng, Y., Hu, J., Chen, J., Mei, Y., Shen, P., Bamford, D.H., et al. (2012). Temperate membrane-containing halophilic archaeal virus SNJ1 has a circular dsDNA genome identical to that of plasmid pHH205. Virology *434*, 233–241.